Closing the loop: upcycling secondary waste materials into nanoarchitectured carbon composites for the electrochemical degradation of pharmaceuticals

Małgorzata Szopińska[1], Jacek Ryl[2], Mattia Pierpaoli[3*]

[1] Gdansk University of Technology, Faculty of Civil and Environmental Engineering, Department of Environmental Engineering Technology, 11/12 Narutowicza St., Gdansk 80-233, Poland;

[2] Gdansk University of Technology, Institute of Nanotechnology and Materials Engineering, Division of Electrochemistry and Surface Physical Chemistry, 11/12 Narutowicza, Gdansk 80-233, Poland;

[3] Department of Metrology and Optoelectronics, Faculty of Electronics, Telecommunication and Informatics, Gdańsk University of Technology, Gdańsk, Poland.

Abstract

In this study, we demonstrated the application of electrochemical oxidation as a safer and cleaner technology for minimizing the impact of pharmaceuticals in wastewaters, simultaneously mediated by upcycled secondary waste materials (SWMs)-derived electrodes, to further reduce their environmental impact. The modularity, scalability, ease of operation and reliability make electrochemical oxidation an ideal process for the destruction of emerging persistent pollutants; however, their full-scale application is hindered by energy efficiency and the potential release of toxic by-products. Thus, the answer to these issues can be found in the design of tailored multifunctional electrode material. For the first time, SWMs derived from combustion and industrial processes have been employed with the simultaneous dual function of functional fillers, in a polyacrylonitrile fibrous matrix, and as a catalyst for the growth of carbon nanofeatures over the fiber surface, to increase the surface area and charge transfer. Next, the tailored composites were employed as anodes for the electrochemical oxidation of acetaminophen, both in phosphate buffer and in a real wastewater sample. The results suggest

* Corresponding author. Email: mattia.pierpaoli@pg.edu.pl
Department of Metrology and Optoelectronics, Faculty of Electronics, Telecommunication and Informatics, Gdańsk University of Technology, Gabriela Narutowicza 11/12, 80-233 Gdańsk (Poland).

28 that SWMs can substitute costly engineered fillers in carbon-based electrodes and that the

29 absence of reaction by-products (monitored by UHPLC-ESI-MS/MS), together with the low

30 energy consumption, make the tailored fibrous composite electrodes good candidates for the

31 development of safer and cleaner technologies with reduced environmental impact.

32 **Keywords**

33 Advanced Oxidation Process; fly ash; spent foundry sand; chemical vapor deposition; carbon

34 nanomaterial

1. Introduction

36 Utilization is one of the leading strategies for the management of hazardous industrial wastes

37 such as fly ash (FA) and spent foundry sand (FS), thus, developing new pathways to minimize

38 their environmental impact is currently a priority. Moreover, due to the ubiquitous presence

39 and persistence of pharmaceuticals and recalcitrant pollutants in the environment, the

40 development and implementation of efficient and cost-effective technologies to mineralize

41 such treats are of primary interest.

42 FA is a particulate material produced from the controlled combustion of fuels, biomass or

43 waste in thermal power plants and it constitutes a major concern for the environment, as it

44 causes water, soil, and air pollution, and because of its costly disposal as a hazardous waste

45 (Wang et al., 2019). For these reasons, diverting FA from landfills, where it also poses a

46 significant threat to the environment, thus finding new pathways for its utilization from the

47 perspective of the circular economy, also finds support in the European Commission guidelines

48 (Gharfalkar et al., 2015). FS is a by-product resulting from the ferrous and nonferrous metal

49 casting industries; it consists of high-quality silica particles, it has low absorption capacity, and

50 it is non-plastic. The spent foundry sand is either recycled in non-foundry applications or

51 landfilled. Indeed, the use of spent FS (originated only from iron, steel, and aluminum foundry

52 operations) has found application in manufactured soils, soil-less potting media, roadway

53 subbase, and as an aggregate for concrete production (Siddique and Singh, 2011), despite it

54 potentially containing heavy metals, and hazardous organics, such as polycyclic aromatic

2

55   hydrocarbons (PAHs), benzene, toluene, xylene (BTEX), polychlorinated-p-dioxins (PCDDs),

56   the related furans (PCDFs) and polychlorinated biphenyls (PCBs) (Environmental Protection

57   Agency, 2014).

58   Acetaminophen (APAP) is the most widely available and prescribed analgesic and antipyretic

59   pharmaceutical in the world, and its presence in the environment has started raising global

60   concerns (Zhang et al., 2018) since it easily accumulates in the aquatic environment, and has

61   been detected in surface waters, wastewater, and drinking water, and also because of its toxic

62   metabolites and hazardous degradation by-products (Wu et al., 2012; Pacheco-Álvarez et al.,

63   2022). While electrochemical oxidation has also been applied to the removal of APAP, the

64   formation of intermediates such as hydroquinone, p-aminophenol, p-nitrophenol, and p-

65   benzoquinone (Li et al., 2014; Zhang et al., 2022) has been reported, and these constitute a

66   potential threat to the environment because of their toxicity and difficulty to degrade (Li et al.,

67   2014; Al-Gharibi et al., 2021). For this reason, optimizing the degradation process, focusing on

68   energy efficiency, and tuning the reaction pathway can be done by intelligently tailoring the

69   material chemical structure and morphology at different scales.

70   Electrochemical oxidation is a reliable and effective water remediation technique for the

71   mineralization of a plethora of water pollutants of current concern, among per- and

72   polyfluoroalkyl substances (PFASs) (Pierpaoli et al., 2021c), pharmaceuticals, dyes and

73   herbicides (Martínez-Huitle and Panizza, 2018; Brillas, 2021; Santos et al., 2021), even in

74   complex and heavily concentrated matrices (Pierpaoli et al., 2021b). In our previous studies,

75   we demonstrated how intelligently nanoarchitectured carbon hybrids possess superior

76   efficiency in micro- and macro-pollutant degradation, due to both their morphology and

77   chemical composition (Pierpaoli et al., 2021b), and that the chemical vapor deposition

78   technique constitutes a preferential path toward the development of highly efficient, critical

79   raw material (CRM)-free electrodes suitable for the designed process (Pierpaoli et al., 2020).

80   Among different carbon allotropes, graphite electrodes are one of the most widely investigated

81   electrode materials in the scientific literature, due to their low cost, availability, and non-

82   toxicity; however, their effectiveness is limited due to their high corrosion rate at potentials

83   higher than 1.7–1.9 versus SCE (Shestakova and Sillanpää, 2017). On the other hand, boron-

3

84 doped diamond electrodes (BDD) are known for their chemical and mechanical inertness, wide

85 potential window, and ability to generate strong oxidants (Martínez-Huitle and Panizza, 2018),

86 which makes them suitable for full-scale applications; however, commercially-available BDD

87 are usually grown by CVD on CRM-containing substrates, such as Nb, with direct effect on the

88 cost and sustainability. For this reason, alternative solutions charting a path towards greater

89 sustainability and lower impact are a major issue. Graphene-based electrodes have only been

90 developed in the last two decades, mostly by a bottom-up approach, being able to define a new

91 class of electrode materials characterized by intermediate properties, and able to adsorb and

92 degrade electrochemically a plethora of pollutants of emerging concern. Cui et al. fabricated a

93 three-dimensional carbon brush using reduced graphene oxide through simple one-step

94 electrodeposition and employed it as a cathode in a bio-electrochemical system for the removal

95 of the azo compound (AO7) (Cui et al., 2018). They attributed the enhanced conductivity and

96 increased electrochemical surface area to the improved AO7 removal efficiency. Similarly,

97 Ormeno-Cano and Radjenovic realized porous boron and nitrogen-doped graphene-based

98 sponge electrodes for the electrodegradation of selected antibiotics, attributing plane the

99 enhanced removal to the strong π-π interactions between the antibiotics and the graphene

100 basal (Ormeno-Cano and Radjenovic, 2022). The inclusion of different nano- and micro-fillers

101 into carbon fibers is generally beneficial to enhancing the mechanical and electrical properties,

102 both inherited by the filler itself and due to their intrinsic catalytic properties. Indeed,

103 Rajabpour and coworkers demonstrated how a graphene sheet can act as a seed to expedite the

104 alignment of all-carbon rings and can be responsible for enhancement of the mechanical

105 properties (Rajabpour et al., 2021).

106 For these reasons, in this study, novel carbon mesostructured electrodes were

107 synthesized for the first time by a simple phase inversion technique combined with a single

108 carbonization-surface decoration step performed in a CVD reactor. Hazardous secondary

109 materials (HSMs) were incorporated into the electrode bulk with the aim of both reducing their

110 environmental impact, by diverting them from landfilling, and acting as catalysts for the

111 development of nano/micro-sized carbon structures on the electrode surface. A comparison

112 with commercially-available graphene oxide flakes and diamonds fillers was also performed.

113 Finally, the acetaminophen degradation efficiency was evaluated for the different architectured

114 electrodes, both in phosphate buffer solution and in a real treated wastewater effluent, aiming

115 to simulate their utilization as an advanced tertiary treatment.

2. Materials and methods

2.1 Materials

118 Polyacrylonitrile (PAN) and APAP (purity >98%) were purchased from Merck.

119 Dimethylformamide (DMF, pure p.a) was bought from POCH (Poland). Phosphate buffer

120 solution (PBS, 0.1 M) was prepared as described in our previous work (Pierpaoli et al., 2021a).

121 Pharmaceutical standard (analytical standard grade) acetaminophen was purchased from

122 Sigma-Aldrich (USA). A stock solution of $500 mgL^{-1}$ and a working solution of $100 mgL^{-1}$ for

123 method calibration were prepared in LC-MS grade methanol (Optima, Fisher Scientific) and

124 stored at -20 °C. Acetonitrile (ACN, LC-MS grade Optima) and formic acid (98–100%,

125 LiChropur for LC-MS) were purchased from Fisher Scientific and Sigma-Aldrich (USA),

126 respectively. Purified water (ultrapure water, resistivity 18.2 $M\Omega$ cm at 25 °C) was obtained via

127 a Direct-Q® Water Purification System. The composition of the treated wastewater (TWW)

128 was analyzed using the methods described in our previous work (Pierpaoli et al., 2021c).

129 Table 1 – Treated wastewater characteristics [mean±standard deviation]

	Parameter	Value
Organic matter characteristics	COD [mg L^{-1}]	34.0±2.1
	BOD$_{20}$ [mg L^{-1}]	<LOD
	TSS [mg L^{-1}]	3.2±0.1
	MSS [mg L^{-1}]	1.6±0.1
	VSS [mg L^{-1}]	1.6±0.1
Nitrogen forms	N-NH$_4^+$ [mg L^{-1}]	0.103±0.015
	N-NO$_3^-$ [mg L^{-1}]	4.69±0.50
	N-NO$_2^-$ [mg L^{-1}]	6.11±0.61
	TN [mg L^{-1}]	10.10±0.81
Phosphate forms	P-PO$_4^{3-}$ [mg L^{-1}]	0.62±0.25
	TP [mg L^{-1}]	0.768±0.016
Other ions	Cl$^-$ [mg L^{-1}]	86.6±2.1
	SO$_4^{2-}$ [mg L^{-1}]	37.9±1.8

	S^{2-} [mg L^{-1}]	<0.1
Basic physicochemical parameters	pH	8.37±0.10
	redox [mV]	187.8±9.8
	Conductivity [mS cm^{-1}]	1164±2.2
Selected micropollutants	APAP [μg L^{-1}]	<LOD

Abbreviations: COD – chemical oxygen demand, BOD – biological oxygen demand, TSS – total suspended solids, MSS – mineral suspended solids, VSS – volatile suspended solids, TN – total nitrogen, TP – total phosphorus, LOD – limit of detection

2.2 Creation and characterization of polymeric electrodes

A solution of 10%w PAN in DMF was prepared and stirred for 24 hours, then a selected filler (Table 2) was added into the mixture and vigorously stirred by a vibration shaker (Vibration stirrer ZX4 Vortex Mixer Velp) until a homogenous solution was obtained.

Table 2 – Description of the fillers used in bulk in the composite realization

Filler name	Filler type	Filler description	Filler dimensions
ND	Diamonds suspension	Commercially available micro-sized diamond suspension	0.6–1.3 μm
GO	Commercial graphene oxide	Commercially available flat graphene oxide flakes	0.2–2.8 μm
FA	Biomass fly ash	Fly ash from a biomass source, obtained from an oxidating atmosphere process	1.7–3.0 μm > 7.5 μm
FS	Foundry sand waste	Foundry sand used in a casting process at a temperature of up to 1400 °C	60–140 nm 140–830 nm > 5 μm

In the case of ND, firstly, a dispersion of ND in dimethylformamide (DMF) was prepared by repeatedly centrifuging and replacing the original solvent (dimethylsulfoxide, DMSO) and finally sonicating. Due to the poor dispersion stability, the PAN was directly added to the ND/DMF solution and vigorously stirred until the polymer extruded in a water-based coagulation bath. Composite electrodes were obtained by the wet-spinning method, using an in-lab made apparatus, then compressed into cylinder electrodes, stabilized, and carbonized by CVD. The detailed procedure can be found in our previous work (Pierpaoli et al., 2022). Simultaneous carbonization and nanofeatures growth were performed by a microwave plasma-

assisted chemical vapor deposition (MWPECVD) system (SEKI Technotron AX5400S, Japan). During the CVD process, which lasted for 40 minutes, the microwave power and the total pressure were kept at 1100 W and 40 Torr, respectively. The substrate holder temperature was set at 550 °C. A gas mixture of H_2, CH_4, and B_2H_6, with a total flow of 328 sccm, was used for the BDD growth. After the fiber wet-spinning procedure and stabilization process in cilindrical mold, flattened cylindric-shaped electrodes, having diameter of 9.45mm (SD=1.0mm) and thickness of 2.0mm (SD=0.17mm) are produced, for a total area of approximately 2 cm^2 (1.96 ± 0.42 cm^2). After carbonization/CVD-growth process, different shrinkage occurs dependently on the filler employed, resulting in a decrease of the electrode geometrical area (ranging between 30% for the only PAN to 7% for the FA) but in an increase of the total exposed one. Scanning electron microscopy (SEM) imaging was carried out using an FEI Quanta 250 FEG (ThermoFisher Scientific) equipped with a Schottky field emission gun and operating with secondary electrons under a 20 kV accelerating voltage. X-ray Photoelectron Spectroscopy (XPS) analyses were done with an Escalab 250Xi (ThermoFisher Scientific) multispectroscope. The spectroscope was operating with an AlKα X-ray source and a spot diameter of 650 μm. The pass energy through the hemispherical analyzer was set to 20 eV. The charge compensation was guaranteed by a low-energy electron and low-energy Ar^+ ion flow, with a final peak calibration at adventitious C 1s at 284.6 eV. Raman spectra were acquired using a commercial Raman microscope (LabRam Aramis, Horiba) on excitation by a 632.8 nm HeNe laser with up to 20 mW optical power at the sample. An integration time of 5 s (20 averages) with a diffraction grating of 300 lines per mm was set, using a 50x magnification objective. All of the peaks were fitted with Lorentzian functions after the spectra were baseline subtracted. Peak ratios were calculated by considering their area, instead of intensity, due to the heterogeneity of the composite material. An Inductively Coupled Plasma – Optical Emission Spectroscopy (ICP-OES) analysis was carried out to assess the presence of metals in trace quantities from the SWMs after performing an acid (HNO_3/HCl 1:3 solution) digestion procedure. The electrochemical properties of the electrode were measured by a VMP-300 BioLogic potentiostat, in a three-electrode cell configuration, in which the BDD, a platinum wire, and an Ag/AgCl 3M KCl electrode were used, respectively, as the working, counter and reference

electrodes in PBS 1M as the electrolyte. The EIS experimental data was fitted using the

BioLogic EC-lab software.

2.3 Electrochemical oxidation setup

Electrochemical oxidation batch tests were performed in a completely stirred borosilicate

beaker as reactor, with an initial volume of 35 mL, in which the electrode sample is completely

immersed (Fig. S1). Twenty minutes after the APAP solution was added to the reactor, to

distinguish the adsorption phase from the oxidative, a 2 mL sample was taken from the beaker

and a constant voltage of +3 V was applied to the electrode. At 5, 15, 30, and 60 minutes,

samples having a volume of 1 mL each were taken and directed to an ultra-high performance

liquid chromatography tandem mass spectrometry with electrospray ionization (UHPLC-ESI-

MS/MS) analysis. The current density was measured during the process. Chemical analyses of

the APAP were performed by UHPLC-ESI-MS/MS (UHPLC Nexera XR coupled with LC/MS-

8050, Shimadzu Company) using an external calibration method. Shim-pack SP-C18, 2.1 x 150

mm, and 2.7 µm was used as an analytical column. A gradient flow was applied starting at 0.15

mlmin^{-1}, ramped up to 0.25 mlmin^{-1} over 4 min, kept at this level until the 9.5 min mark, then

returned to 0.15 ml (11 min), and maintained here until the 12 min mark. A gradient mobile

phase was used; starting at 95% mobile phase A (0.3 % formic acid in ultrapure water, and 5%

of mobile phase B (1:1 MeOH, ACN, solution) kept until the 4 min mark, followed by a linear

increase over 8 min to 65% A and 35% B, a second increase to 100 % B at the 9 min mark,

maintained until 9.5 mins. (washing stage), then returned to the initial conditions (11 min

mark), and held for 1 min (re-equilibration to initial condition). The column temperature was

maintained at 40 °C and the autosampler at 4 °C. The total run time was 12 min. LC eluate was

sprayed into a tandem mass spectrometer by electrospray ionization in the positive ion mode.

The interface setup parameters were as follows: nebulizing gas flow (N2, 2 Lmin-1), heating

gas flow (N2, 8 Lmin^{-1}), interface temperature (150 °C), desolvation temperature (261 °C), heat

block temperature (400 °C). The APAP eluted at 6.75±0.05 min and was a monitored by

multiple reaction monitoring (MRM) transition m/z 152.0 > 110.2 (collision energy (-17 eV);

quantifier transition) and m/z 152.0 > 65.2 (collision energy (-29 eV); qualifier transition).

MOST WIEDZY Downloaded from mostwiedzy.pl

204 Potential APAP oxidation products include hydroquinone (ESI+, MS m/z=123), p-
205 benzoquinone (ESI+, MS m/z=121), ketomalonic acid (ESI+, MS m/z=119), maleic acid (ESI+,
206 MS m/z=117), oxalic acid (ESI+, MS m/z=91), oxamic acid (ESI+, MS m/z=90), and acetamide
207 (ESI+, MS m/z=60), and were evaluated using scanning single ion monitoring mode (SIM)
208 under the same chromatographic conditions after Li et al. (Li et al., 2014). The sample injection
209 volume was 1 µL. The calibration curve was plotted using 5-level calibration (linearity 1–1000
210 µgL^{-1}. The method detection limit (MDL) and method quantification limit (MQL) were 1 and 3
211 µgL^{-1} and 1.5 and 4.5 µgL^{-1} for water and wastewater matrix, respectively. For this method, no
212 analyte pre-concentration was applied. To evaluate the APAP removal efficiency as function of
213 the energy consumed, the specific electrical charge (Q) is reported as follow: Q=Jt/V where Jt
214 is the integral of the measured current over time (A*h) and V is the solution volume (L)
215 (Anglada et al., 2009). Since the applied potential is constant, Q is directly proportional to the
216 power used.

217 ## 3. Results and discussion

218 ### 3.1 Electrode characterization

219 Due to their nature as combustion products, FA and FS do not possess a well-defined
220 morphology and chemical composition, but they are rather dependent on the combustion
221 process parameters and feedstock composition. For this reason, a more in-depth analysis was
222 performed to characterize the waste materials. From Fig. 1a, it is possible to observe the
223 presence of both spherical and irregularly shaped particles.
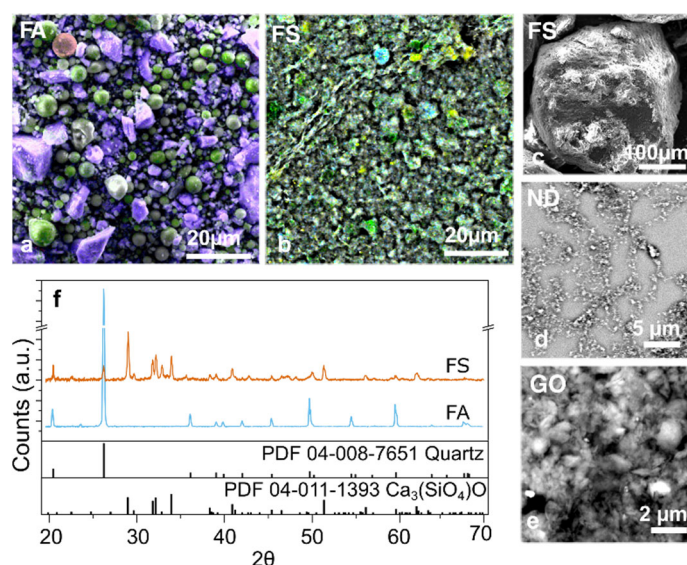
Fig. 1 – SEM-EDX pictures of (a) FA (in yellow aluminum silicates, in blue calcium silicates and in red Fe-rich particles; (b) fine fraction of FS (in green calcium carbonates, in yellow calcium silicates and in blue Fe-rich) and (c) large fraction of FS. SEM of (d) ND solution dried on Si substrate; (e) GO flakes, and XRD diffractograms of FS and FA. The reader is referred to the web version of this paper for the color representation of this figure.

In particular, a bimodal particle size distribution is present in the FA sample, with the smaller fraction accounting for particles having a diameter between 1 and 3 μm and the larger one having an equivalent diameter larger than 8 μm. FS is mostly constituted by subangular sand with obtuse angles, with a diameter ranging from tens to hundreds of micrometers (Fig. 1c) and a superfine fraction (0.05–1 μm, Fig. 1b), which results from the presence of inorganic and organic binders, and other additives used during the casting process (Siddique and Singh, 2011). Quartz and calcium silicate are the prevalent crystalline form (Fig. 1e); however, Al is predominant as well, as determined by the EDX analysis, and other elements are present in minor quantities, as reported in Table S1. Indeed, a major difference arises between FA and FS, related to the Fe content, especially after acid treatment, suggesting a different composition (Table S2). The commercial ND suspension presents particles agglomerating into larger structures (Fig. 1d), as well as for the graphene oxide flakes (Fig. 1e).

GO, NDs, FA and FS were then added to the PAN/DMF solution, and the electrodes were

10

244   synthesized. SEM images of the different electrode composites, after CVD-carbonization, are

245   reported in Fig. 2.
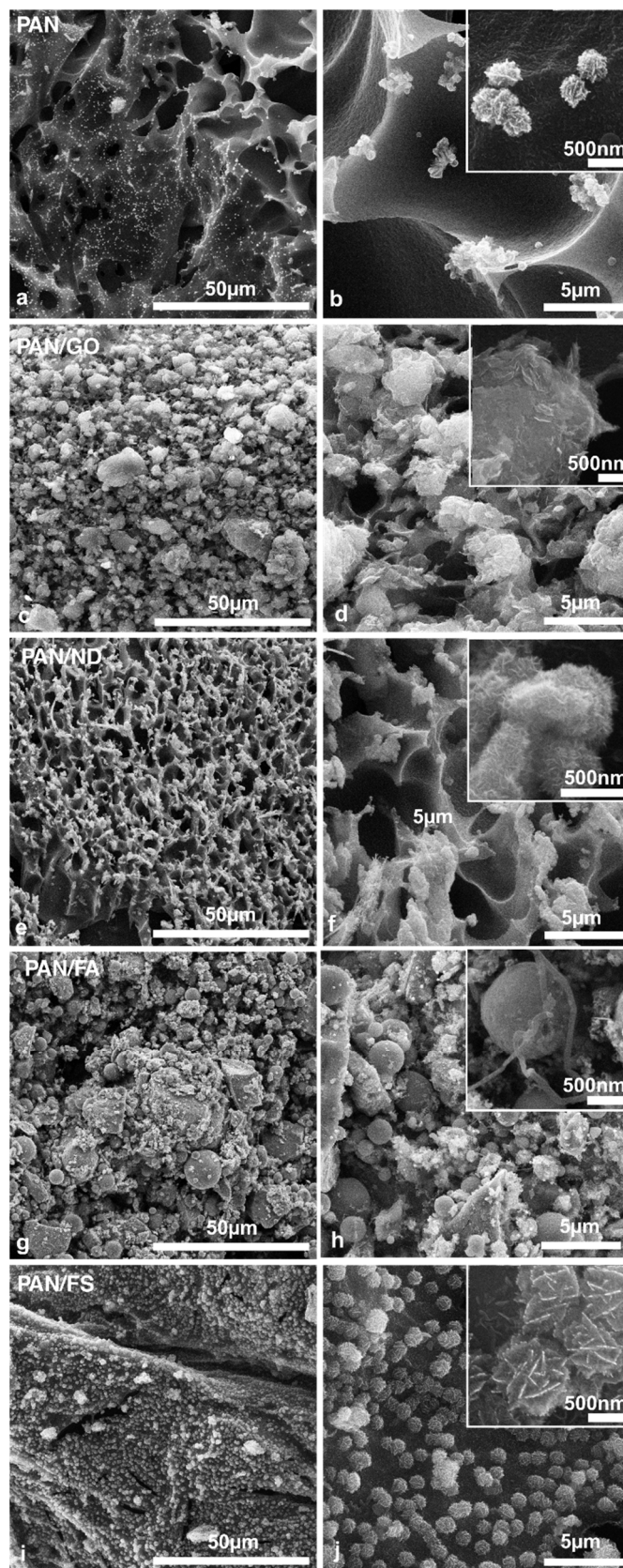
246

247   *Fig. 2 – SEM of the differently synthesized composite materials before the oxidation tests.*

11

248 It is possible to observe the characteristic fiber morphology in Fig. 2a, obtained by the

249 combined action of phase inversion during the wet-spinning process, and the effect of the

250 plasma in etching the outer fiber interfacial layer. A few micrometer-sized carbon nanowalls-

251 flakes are present on the pores' edges as a result of the locally-enhanced plasma during CVD

252 (Fig. 2f). The addition of different powders dramatically affects the composite morphology. For

253 both GO and NDs, it is still possible to observe a similar porous structure, which is more open

254 for the PAN/ND composite, while it is partially clogged by the GO flakes in the case of PAN/GO

255 (Fig. 2g), where it is possible to observe the presence of the wrinkled graphene sheets on the

256 composite surface. Indeed, the GO flakes hinder the transport of ionic species toward the PAN

257 microporous structure, as also demonstrated by the electrochemical characterization, in Fig.

258 3. The presence of NDs leads to the formation of a highly developed agglomerated structure

259 during the CVD process constituted by tiny carbon nanowalls (Fig. 2h). The presence of

260 different carbon architectures in the PAN/FA composite is the result of the FA chemical

261 heterogeneity. In particular, it is possible to observe both amorphous carbon and the formation

262 of fibers and nanotubes, catalyzed by the presence of Fe within FA (Fig. 2i). Nevertheless, in

263 the PAN/FS composite, most of the larger particles have sedimented in the spinning solution,

264 thus only the finer FS fraction is present in the composite; moreover, it is interesting to observe

265 the formation and a high density of nanowall-coated spherical structures which cover most of

266 the fiber surface, with a very limited porosity (Fig. 2j).

267 The electrochemical behaviors of the different carbon electrodes were systematically tested in-

268 situ, using the same reactor for the APAP EO tests. Fig. 3a–e reports the voltammograms at

269 different scan rates for all five of the composites in 1M PBS, at a potential window from 0 to

270 0.4 V. The CV curves of bare PAN, PAN/ND, and PAN/FS composites present the characteristic

271 shape of an electrochemical double-layer capacitor (EDL). The large rectangular-shaped area

272 for these two composites suggests better electrolyte penetration in the pores compared to the

273 PAN/GO and PAN/FA. Indeed, in the later ones, at high scan rates, an oval-shaped resistive-

274 capacitive behavior is observed, which is related to a high instability of EDL and the poor

275 capacitive nature of the electrodes. The main factor affecting ionic diffusion within the porous

276 structure of carbon materials is the structure of the porous network itself. By plotting current

277 versus the scan rate, straight interpolating lines were obtained, to estimate the EDL

278 capacitance values (Fig. S2).

279
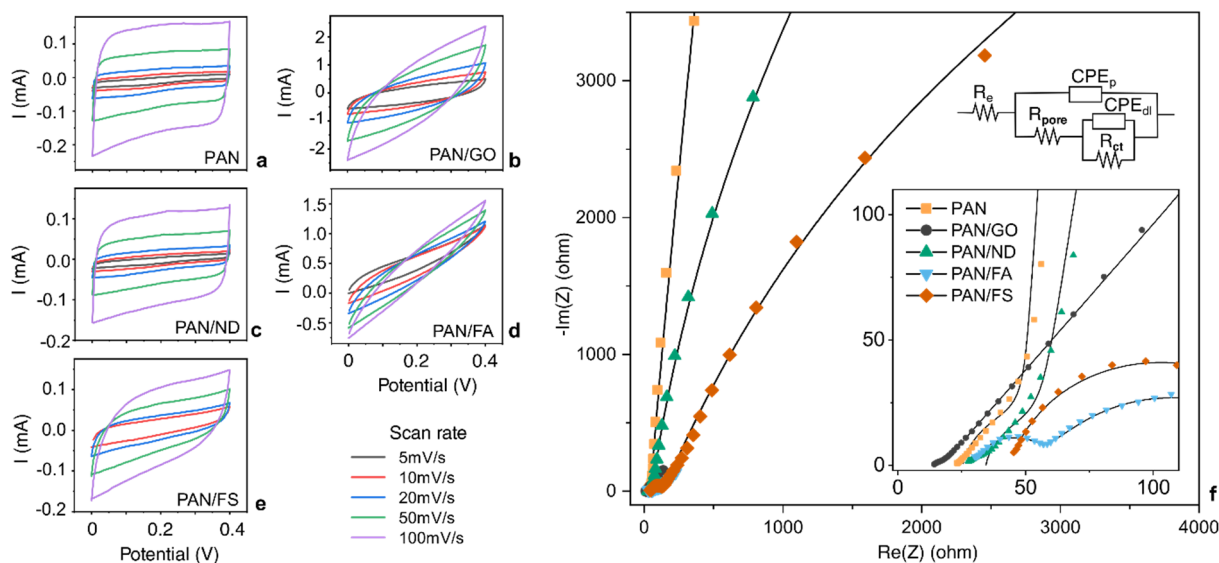
281 *Fig. 3 – (a–e) Cyclic voltammograms at different scan rates for all 5 composites in 1M PBS, at a*

282 *potential window from 0 to 0.4 V. (f) EIS Nyquist plot. Straight lines are results of EEC fit. The*

283 *reader is referred to the web version of this paper for the color representation of this figure.*

284 To further examine the interfacial charge transport dynamics of the synthesized composite

285 electrodes, electrochemical impedance spectroscopy (EIS) was employed. Fig. 3f shows the

286 Nyquist plots, highlighting the different behaviors across the 200 kHz – 20 mHz frequency

287 range. The obtained semicircles were fitted with an equivalent electrical circuit (EEC) model,

288 reported in the inset, which includes the solution resistance (R_s), pore resistance (R_p), pore

289 capacitance (CPE_p), charge transfer resistance (R_{ct}), and double-layer capacitance (CPE_{dl}); the

290 fitted parameters are tabulated in Table S4. Unexpectedly, despite the different origin and

291 chemical composition of the powders, their incorporation within the PAN composite was found

292 to have a minor effect on the conductivity of the electrode, as described by the comparable

293 value of R_s, equal to 30±15 Ω. The reason for such a finding may be that the CVD-growth

294 electrode surface constitutes the preferential path for the charge transfer rather than the fiber

295 bulk. Indeed, the lowest R_s belongs to the PAN/GO, for which stacks of GO flakes are

296 recognizable from the SEM picture (Fig. 2g). Similarly, the first semicircle in high-frequency

13

297   regions is easily distinguishable for all of the samples, which is attributed to the combined

298   effect of charge transport resistances at the electrode/electrolyte interfaces (R_{ct}). At a first look,

299   PAN, PAN/ND, and PAN/FS exhibit similar behavior and they fit the EEC well, characterized

300   by a large semicircle at low frequencies related to the bulk Nernst diffusion. However,

301   examining the different Nyquist plots individually, the smaller semicircle at high frequencies

302   indicates a faster ionic transference within the EDL for the PAN/GO sample, followed by a

303   linear response in the low-frequency region, resulting in an angle of 45° with the axis, which

304   corresponds to low ionic diffusion resistance (well-represented by a Warburg element

305   (Randles, 1947). EDL capacitance values obtained from CV and EIS studies were compared

306   and used to estimate the electrochemical surface area (ECSA), since this method allows for

307   accounting the total surface accessible to the solution. ECSA was estimated utilizing the

308   relationship ECSA = C_{dl} / C_S, where C_S is the specific capacitance of the investigated material.

309   However, the exact C_S value is typically unknown, leading to substantial errors in ECSA

310   determination from CDL. It is commonly accepted to use a single C_S value for ECSA for

311   comparative purposes, yet the numbers obtained this way may be under- or overestimated

312   (Morales and Risch, 2021; de Freitas Araújo et al., 2022). For comparison, we considered 0.06

313   mF cm^{-2} based on the previous literature reports for porous carbonaceous materials (de Freitas

314   Araújo et al., 2022). The estimated ECSA it is between 16 cm^2 for PAN and ND and almost

315   double for FA and FS (22 and 34 cm^2 respectively), while for GO is 150 cm^2, which could be

316   overestimated.

317 The Raman spectra presented in Fig. 4a show the difference between the different composites,

318 before and after the EO tests. The spectra were deconvoluted and the peak was analyzed, by

319 considering bands at 1577 (9), 1337 (6), 1612 (8), 1493 (12), and 1189 (12) cm^{-1} (standard

320 deviation in brackets), attributed to the G (graphitic, attributed to E_{2g} phonon vibrations of sp^2

321 carbon atoms), D (corresponding to the A_{1g} breathing mode, attributed to the disorder-induced

322 defects), D' (appearing as a shoulder of the G peak, observed in microcrystalline graphite and

323 glassy carbon), D* (a broad band, attributed to amorphous carbon and to the presence of

324 hetero-atoms as impurities in the carbon lattice) and D'' (trans-polyacetylene) bands (Lee et

325 al., 2022).

14
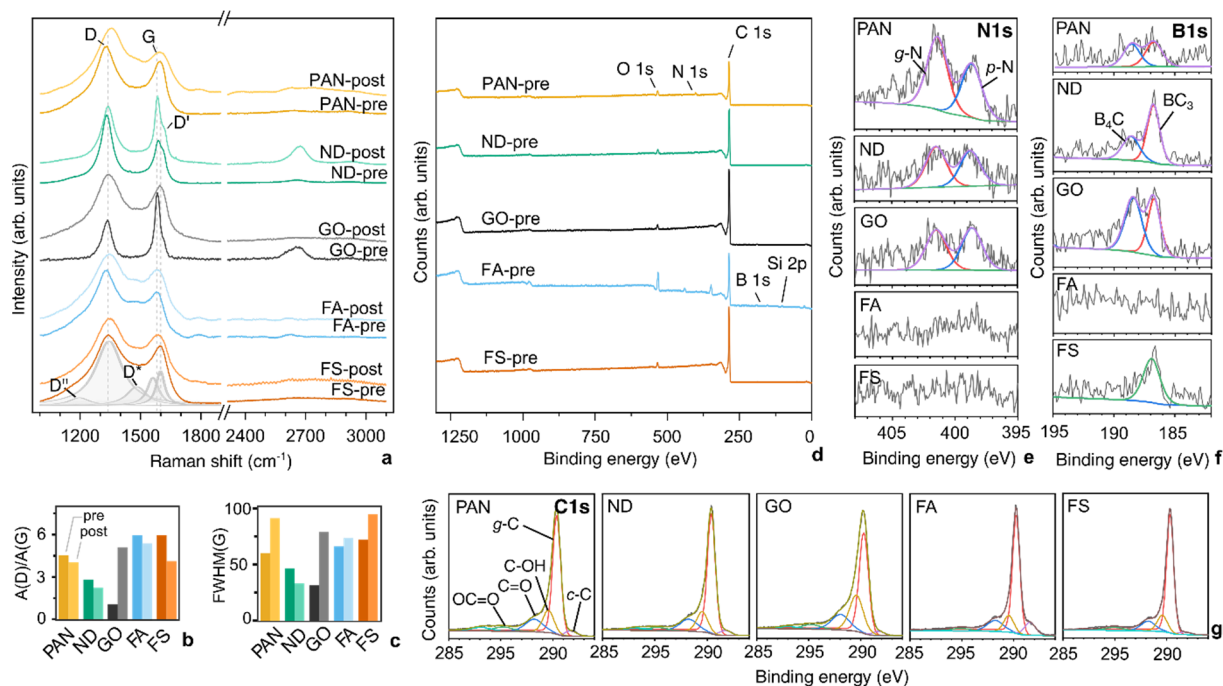
Fig. 4 – (a) Raman spectra, with an example of the peaks used for the deconvolution, (b) A(D)/A(G) ratios, (c) FWHM(G) of the samples before and after EO tests. (d) A(D)/A(G) versus ratio A(D')/A(G). X-ray photoelectron spectroscopy (XPS) spectra of the different samples: (d) survey spectra; (e) N 1s spectra; (f) B 1s spectra; and (g) C 1s spectra. The reader is referred to the web version of this paper for the color representation of this figure.

The position, intensity (relative to the G-band, expressed as a ratio) and broadening of the D band depends on the type of disorder, the presence of impurities, and functional groups. The intensity ratio of A(D)/A(G) is commonly used as an estimator of the defect density in carbon materials since it is sensitive only to defects in the rings. In particular, the relative peak intensity, expressed as the ratio of the integrated area of the D and D' bands, has been preferred because the area under the band represents the probability of the whole scattering process (Martins Ferreira et al., 2010; Del Corro et al., 2014). Firstly, by comparing the A(D)/A(G) of the different composites, before EO, it is possible to observe that the ratio is lower for the composites containing ND and GO. Thus, the presence of such engineered carbon nanofillers may improve the formation of a large ladder structure, being converted into a large graphene layer. All of the samples, with the exception of the PAN-GO, show a slight decrease in the A(D)/A(G) ratios after the EO tests (Fig. 4b and Table S4), which can probably be attributed to

15

344 the oxidation and elimination of amorphous and disordered carbons, leaving exposed the

345 better-crystallized fiber surface, as also supported by their FWHM(G). It is interesting to

346 observe that the biggest difference belongs to the PAN/GO sample, already visible by

347 qualitatively comparing the spectra (Fig. 4a). In contrast, the A(D)/A(G) ratio for the PAN/ND

348 sample after EO is significantly lower than the others. On the other hand, the FWHM of the G

349 peak always increases for the increasing disorder, since this parameter is sensitive to all types

350 of defects, either in the sp^2 rings or chains (Eckmann et al., 2013), making it a good indicator

351 of the degree of graphitization of carbonaceous materials. Thus, the widening of the D and G

352 peaks after the EO process (Fig. 4c) was also observed in our previous studies (Pierpaoli et al.,

353 2021b) for sp^2-C-rich carbon nanoarchitectured electrodes, while almost no difference was

354 found for boron-doped diamond ones. Indeed, it is interesting to find that the PAN-ND

355 composite belongs to the lowest FWHM, probably due to the beneficial effect of NDs within

356 the structure of the fiber acting as nucleation seeds, in a similar fashion as reported by

357 (Rajabpour et al., 2021).

358 Furthermore, XPS was performed on CVD-carbonized PAN composites to quantify the

359 differently hybridized carbon and functional groups. XPS survey spectra are shown in Fig. 4d.

360 The N1s XPS spectra were deconvoluted into two peaks: at around 398.7 eV, attributed to

361 pyridinic N, and at around 401.5 eV, corresponding to graphitic N. The presence of the pyrrolic

362 N peak can overlap the graphitic N; however, due to the low N content (< 4%), it is difficult to

363 distinguish the peaks, especially for the PAN-FA and PAN-FS composites, for which a higher

364 amount of fillers is present. Thus, it is possible to affirm that the nitrogen is related to the bare

365 PAN structure, differently from the boron which is associated with the nanostructure growth,

366 due to the introduction of B_2H_6 during the MPECVD process. Indeed, it is also possible to

367 qualitatively compare the grown nanostructure by the SEM reported in Fig. 2, with the

368 presence of the B1s profiles. The B1s profiles shown in Fig. 4f indicate that several B species

369 are present and incorporated within the CVD-grown nanostructure, and the two peaks, at

370 approximately 188.6 and 186.8 eV, could correspond to B_4C and BC_3, respectively (Bepete et

371 al., 2013). The BN peak is not present (191 eV), due to the low N content, limited to the PAN

372 fiber, and not available as a gas precursor, while the presence of B_4C is inhibited in the PAN-

16

373   FS composite. Finally, the C1s spectra (Fig. 4g) show five peaks after deconvolution. The peak

374   at 284.7 eV corresponds to graphitic carbon. The peak at 283.3 eV can be associated with the

375   carbidic components (SiC, BC) for the PAN/FS and PAN/FA composites. The peak at 285.4 eV

376   is likely to arise from the graphene domain edges and defects, or by C-OH. The higher binding

377   energy peaks at ca. 286.8 and 289.9 eV are attributed to the formation of C–O bonds. For a

378   quantitave comparison, fitted results of C1s, N1s and B1s core level XPS spectra for the different

379   composite electrodes are reported in Table S5.

380   **3.2 Electrochemical oxidation tests**

381   The oxidation of organic compounds by electrochemical technique involves two different

382   mechanisms acting simultaneously: direct anodic and indirect oxidations. In the first, the

383   electron transfer between the organic compound and the anode occurs directly on its surface,

384   while in the indirect oxidation, the electrochemical process is mediated by highly reactive

385   oxidant generated by the reaction with other species (e.g. hydroxyl radical, chlorine active

386   species), which are electro-generated at the anode surface (Martínez-Huitle and Panizza, 2018;

387   Wilk et al., 2022). Moreover, secondary oxidants reactive sulfate species (sulfate radicals,

388   peroxydisulfates) at appropriate current density may also occurs during EO (Ganiyu et al.,

389   2021). Possibility of their in-situ EO generation, especially in sulphate-reach matrix constitute

390   additional influence for effective degrading organic contaminants. Indeed, $S_2O_8^{2-}$ can be

391   electrosynthesized from the SO_4^{2-} oxidation, resulting, then, in the cathodic production of $SO_4^{\bullet-}$

392   (Araújo et al., 2022) also by sp2-C rich boron-doped diamond hybrid electrodes (de Freitas

393   Araújo et al., 2022). However, considering the relatively low concentrations of chloride and

394   sulphate ions in the studied matrix (Table 1), the contribution of such electrogenerated

395   oxidants, may play a minor role in the mineralization process. However, the anode material

396   plays a predominant role in favoring one or other pathway (Brito et al., 2021). In particular,

397   the higher charger transferability, the larger active surface, and superior stability are

398   preferential for ideal electrode material (Faber et al., 2014). Indeed, it has been reported that

399   B, N co-doping reduces the charge transfer resistance, induces high electrical conductivity, and

400   fosters quicker EOP kinetics (Zhang et al., 2020).

401 To oxidize APAP on gassy carbon electrodes, a potential ranging between 0.2 and 0.7 V vs SCE

402 should be applied to the anode, depending on the solution's pH, as has been reported

403 (Nematollahi et al., 2009). However, a higher applied potential may be necessary to directly

404 transfer electrons from the APAP to the anode, and to allow the formation of different oxidants.

405 Moreover, the APAP oxidation pathway is known to follow complex kinetics, due to the variable

406 OH concentration caused by the parallel consumption of this oxidant in fast reactions with

407 products (Brillas et al., 2005). The electrochemical degradations of APAP were evaluated both

408 in phosphate buffer (PB) and treated wastewater (TWW) by the different composite electrodes.

409 **3.2.1 EO in phosphate buffer**

410 Degradation of APAP was quantified as a pseudo-first-order kinetic in PBS (Fig. 5a) and a

411 pseudo-zero-order kinetic in TWW (Fig. 5e), under the application of a +3V vs Ag/AgCL 3M

412 KCl electrode. The initial concentration of APAP was set as 10 mg/L for all of the reported

413 experiments, in a 0.1M PBS. Before the application of a constant potential to the electrode, the

414 solution was stirred with the PAN-based electrode composite and allowed to rest for 20

415 minutes to allow adsorption (Fig. 5c). The presence of a high level of graphitization on the

416 carbon surface seems to play an important role in adsorption, allowing for the π–π interaction

417 with the benzene ring present in the organic molecules (Tian et al., 2020). As can be observed

418 in Fig. 2i, the PAN/FA morphology lacks a porous carbon-rich coating, while it catalyzes the

419 growth of nanofiber-like structures, thus exhibiting the lowest adsorption. To compare the

420 APAP removal efficiencies with the energy consumed, Fig. 5b reports the plot between the

421 efficiency and specific current density, measured during the tests. It is possible to observe that,

422 while the PAN-GO electrode exhibits the faster removal kinetic (Fig. 5a), it also has the highest

423 energy consumption, since part of the energy is consumed by the electrode oxidation, as is also

424 well documented by the big difference in the Raman spectra before and after the EO process

425 (Fig. 4a). For this reason, it was deemed appropriate to compare the angular coefficients of the

426 linear regressions, which express the APAP oxidation efficiency at a specific energy density

427 (Fig. 5b), which have been reported in Fig. 5d. The APAP adsorption, evaluated at the

428 beginning of the tests (Fig. 5c) shows a comparable effect between the different composites,

18

429 except for the PAN/FA sample, which does not show an outer carbon "skin" at the solid/liquid

430 interface, which can be simply explained by the low π−π interactions.
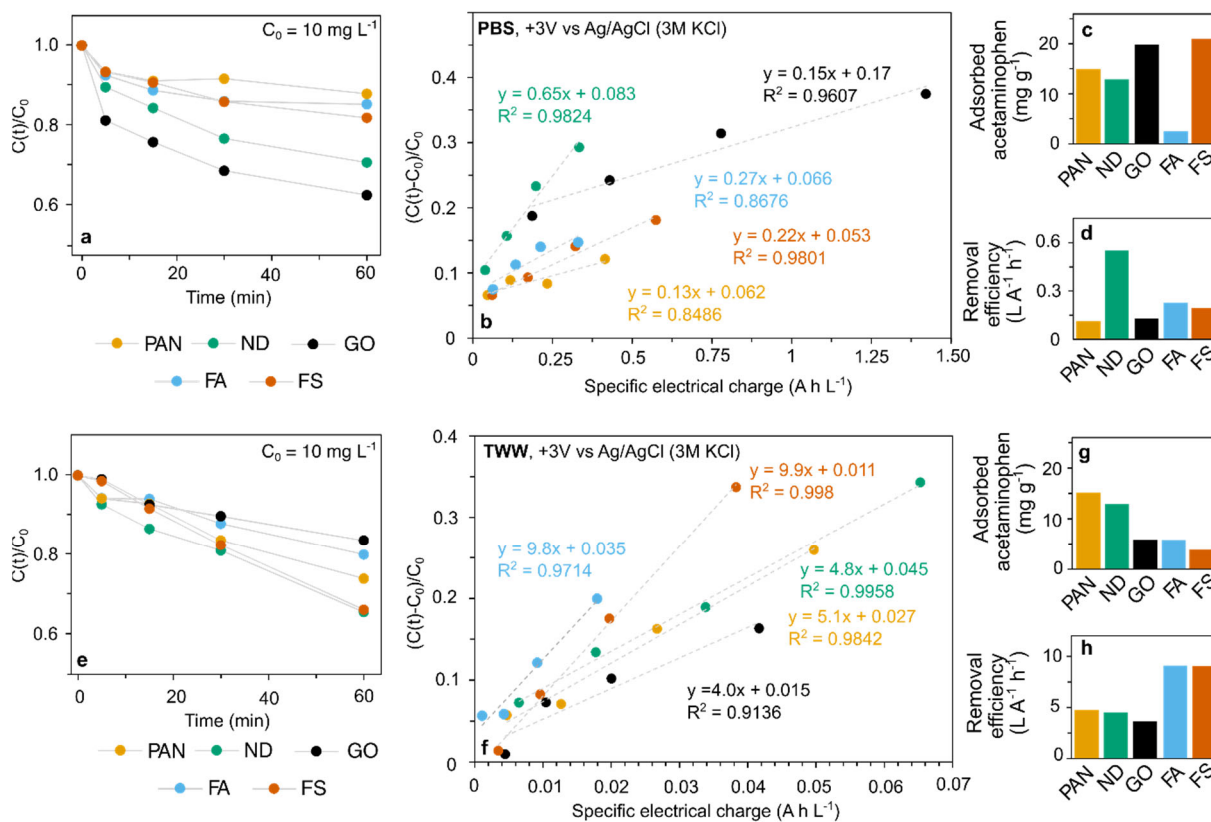
431

432 *Fig. 5 – (a,e) normalized APAP concentration versus time. (b,f) comparison between APAP removed*

433 *and specific energy density measured. (c,g) APAP initially adsorbed by the electrode and (d,h) their*

434 *corresponding removal efficiency in 0.1M PBS at the applied potential of 3 V vs AgAgCl 3KCl. The*

435 *reader is referred to the web version of this paper for the color representation of this figure.*

436 We also further investigated the impact of chloride species on the AC degradation, (PBS

437 containing 0.137 M NaCl, 2.7 mM KCl, 8 mM Na_2HPO_4, 2 mM KH_2PO_4) on the degradation of

438 AC, finding that more than 99% was degraded in the first 5 minutes, for all of the electrodes.

439 The redox chemistry of aqueous chlorine species depends on several experimental conditions,

440 such as the solution pH, which results in the different fractioning of different aqueous active

441 chlorine species. Indeed, during the electrochemical oxidation process, Cl- could be oxidized

442 to Cl_2, Cl_2O, or HClO, all of which indirectly participate in the APAP oxidation reactions (Wilk

443 et al., 2022), thus explaining the abrupt APAP degradation.

19

3.2.2 EO in TWW

To assess the effectiveness of employing the synthesized electrodes for the electrochemical degradation of pharmaceuticals in relevant environments as an advanced treatment, the oxidation of APAP, as a representative widespread drug, from a real TWW matrix was investigated. Firstly, TWW is characterized by a lower conductivity than PBS, which implies an increase in the applied potential for the same current density. On the other hand, the higher potential may result in the formation of different active species that may participate both in the indirect oxidation processes, oxygen evolution, and accelerated electrode degradation; thus, it was decided to apply the same potential, with the result of a lower current density on the electrode, thus a reduced removal efficiency. Similar behaviors were observed in other studies, such as in tap water, due to the lower conductivity (Ormeno-Cano and Radjenovic, 2022) and the absence of organic matter (Pierpaoli et al., 2021c). It is worth reporting that the PAN/ND composite exhibits a higher removal efficiency in PBS (Fig. 5d). BDD electrodes are known to possess a distinct advantage over other electrode materials of their stability, chemical inertness, due to the C atoms in sp^3 hybridization (Martínez-Huitle and Panizza, 2018). Even if their presence was not directly probed on the PAN/ND surface, their presence in the PAN bulk may induce a less defective structure (Fig. 4), therefore resulting in a wider active surface, not limited to the single BDD grain boundaries exposed to the electrolyte. The highest efficiencies attributable to FA and FS (Fig. 5h) may also be attributable to their lower capacitive behavior (Table S4), favoring faradaic processes instead. For both tests, pH increases with time, more remarkably in TWW (from 7.7 to 10.5 after 1h of treatment), rather than PBS (from 7.8 to 8.0).

In summary, both the electrode morphology and the chemical structures play important roles in the APAP degradation: Zhang et al. reported that co-doped atoms and the unsaturated carbon atoms provide a series of potential active sites; in particular, the copresence of B, carrying negative charges due to the strong electronegativity, with C neighboring atoms, represent a preferential site for the adsorption of O and O_2 intermediates (Zhang et al., 2020). Interestingly, no by-products, inc. hydroquinone, p-benzoquinone, ketomalonic acid, maleic acid, oxalic acid, oxamic acid, and acetamide, were identified during the EO processes (Fig. S3,

473   S4).

4. Conclusion

In this study, we demonstrated how to upcycle hazardous waste into architectured electroactive carbon-based electrodes and demonstrated their potential for the oxidation of acetaminophen, as a putative pharmaceutical, in real wastewater. Combustion by-products and industrial waste can be used as inexpensive fillers in polyacrylonitrile-based composites and as catalysts, able to induce the growth of different carbon nanostructures by catalytic chemical vapor deposition. The introduction of fly-ashes and foundry sand waste into the PAN matrix resulted in an acetaminophen electrochemical removal efficiency twice that of the bare PAN-based electrode, which acts differently as a catalyst during the CVD process: while large the Fe-rich particles in the FA catalyze the formation of tubular carbon nanostructures, the complex sub-micron FS fraction enhances the degree of graphitization of the composite electrode. The addition of nanodiamonds, acting as a nucleation seed, positively affect the CVD-grown interfacial structure, resulting in a more ordered graphitic structure, which is related to the fastest degradation kinetics, both in PBS and TWW. On the other hand, the addition of graphene oxide into the electrode is detrimental, since most of the energy is consumed in the electrode oxidation. No by-products, inc. hydroquinone, p-benzoquinone, ketomalonic acid, maleic acid, oxalic acid, oxamic acid, and acetamide, were identified during the EO processes. The most remarkable result of the present study is the demonstration of upcycling hazardous materials into valuable catalysts for the creation of electrodes to degrade hazardous water pollutants. Further investigations are intended to apply the current modulation technique, by continuously adjusting the applied current, to reduce the energy consumption, and develop topologically optimized flow-through electrodes, for developing a more efficient process.

References

Al-Gharibi, M.A., Kyaw, H.H., Al-Sabahi, J.N., Zar Myint, M.T., Al-Sharji, Z.A., Al-Abri, M.Z., 2021. Silver
    nanoparticles decorated zinc oxide nanorods supported catalyst for photocatalytic degradation of

501   paracetamol. Mater. Sci. Semicond. Process. 134, 105994. https://doi.org/10.1016/j.mssp.2021.105994

502 Anglada, A., Urtiaga, A., Ortiz, I., 2009. Contributions of electrochemical oxidation to waste-water treatment:
503   fundamentals and review of applications. J. Chem. Technol. Biotechnol. 84, 1747–1755.
504   https://doi.org/10.1002/jctb.2214

505 Araújo, K.C., dos Santos, E. V., Nidheesh, P. V., Martínez-Huitle, C.A., 2022. Fundamentals and advances on the
506   mechanisms of electrochemical generation of persulfate and sulfate radicals in aqueous medium. Curr.
507   Opin. Chem. Eng. 38, 100870. https://doi.org/10.1016/j.coche.2022.100870

508 Bepete, G., Voiry, D., Chhowalla, M., Chiguvare, Z., Coville, N.J., 2013. Incorporation of small BN domains in
509   graphene during CVD using methane, boric acid and nitrogen gas. Nanoscale 5, 6552–6557.
510   https://doi.org/10.1039/c3nr01699d

511 Brillas, E., 2021. Recent development of electrochemical advanced oxidation of herbicides. A review on its
512   application to wastewater treatment and soil remediation. J. Clean. Prod. 290, 125841.
513   https://doi.org/10.1016/j.jclepro.2021.125841

514 Brillas, E., Sirés, I., Arias, C., Cabot, P.L., Centellas, F., Rodríguez, R.M., Garrido, J.A., 2005. Mineralization of
515   paracetamol in aqueous medium by anodic oxidation with a boron-doped diamond electrode. Chemosphere
516   58, 399–406. https://doi.org/10.1016/j.chemosphere.2004.09.028

517 Brito, L.R.D., Ganiyu, S.O., dos Santos, E. V., Oturan, M.A., Martínez-Huitle, C.A., 2021. Removal of antibiotic
518   rifampicin from aqueous media by advanced electrochemical oxidation: Role of electrode materials,
519   electrolytes and real water matrices. Electrochim. Acta 396, 139254.
520   https://doi.org/10.1016/j.electacta.2021.139254

521 Cui, D., Yang, L.M., Liu, W.Z., Cui, M.H., Cai, W.W., Wang, A.J., 2018. Facile fabrication of carbon brush with
522   reduced graphene oxide (rGO) for decreasing resistance and accelerating pollutants removal in bio-
523   electrochemical systems. J. Hazard. Mater. 354, 244–249. https://doi.org/10.1016/j.jhazmat.2018.05.001

524 de Freitas Araújo, K.C., Vieira dos Santos, E., Pierpaoli, M., Ficek, M., Santos, J.E.L., Martínez-Huitle, C.A.,
525   Bogdanowicz, R., 2022. Diamondized carbon nanoarchitectures as electrocatalytic material for sulfate-
526   based oxidizing species electrogeneration. Electrochim. Acta 430, 1–11.
527   https://doi.org/10.1016/j.electacta.2022.141069

528 Del Corro, E., Taravillo, M., Baonza, V.G., 2014. Stress-dependent correlations for resonant Raman bands in
529   graphite with defects. J. Raman Spectrosc. 45, 476–480. https://doi.org/10.1002/jrs.4475

530 Eckmann, A., Felten, A., Verzhbitskiy, I., Davey, R., Casiraghi, C., 2013. Raman study on defective graphene:
531   Effect of the excitation energy, type, and amount of defects. Phys. Rev. B - Condens. Matter Mater. Phys. 88,
532   1–11. https://doi.org/10.1103/PhysRevB.88.035426

533 Environmental Protection Agency, 2014. Risk Assessment of Spent Foundry Sands In Soil-Related Applications
534   Evaluating Silica-based Spent Foundry Sand From Iron, Steel, and Aluminum Foundries 477.

535 Faber, M.S., Dziedzic, R., Lukowski, M.A., Kaiser, N.S., Ding, Q., Jin, S., 2014. High-performance electrocatalysis
536   using metallic cobalt pyrite (CoS 2) micro- and nanostructures. J. Am. Chem. Soc. 136, 10053–10061.
537   https://doi.org/10.1021/ja504099w

538 Ganiyu, S.O.S.O., Martínez-Huitle, C.A.C.A., Oturan, M.A.M.A., 2021. Electrochemical advanced oxidation
539   processes for wastewater treatment: Advances in formation and detection of reactive species and
540   mechanisms. Curr. Opin. Electrochem. 27, 100678. https://doi.org/10.1016/j.coelec.2020.100678

541 Gharfalkar, M., Court, R., Campbell, C., Ali, Z., Hillier, G., 2015. Analysis of waste hierarchy in the European
542   waste directive 2008/98/EC. Waste Manag. 39, 305–313.

543 Lee, J.E., Choi, J., Lee, D.J., Lee, S., Chae, H.G., 2022. Radial microstructure development of polyacrylonitrile
544   (PAN)-based carbon fibers. Carbon N. Y. 191, 515–524. https://doi.org/10.1016/j.carbon.2022.02.023

545 Li, J., Ye, Q., Gan, J., 2014. Degradation and transformation products of acetaminophen in soil. Water Res. 49,
546   44–52. https://doi.org/10.1016/j.watres.2013.11.008

Martínez-Huitle, C.A., Panizza, M., 2018. Electrochemical oxidation of organic pollutants for wastewater treatment. Curr. Opin. Electrochem. 11, 62–71. https://doi.org/10.1016/j.coelec.2018.07.010

Martins Ferreira, E.H., Moutinho, M.V.O., Stavale, F., Lucchese, M.M., Capaz, R.B., Achete, C.A., Jorio, A., 2010. Evolution of the Raman spectra from single-, few-, and many-layer graphene with increasing disorder. Phys. Rev. B - Condens. Matter Mater. Phys. 82. https://doi.org/10.1103/PhysRevB.82.125429

Morales, D.M., Risch, M., 2021. Seven steps to reliable cyclic voltammetry measurements for the determination of double layer capacitance. JPhys Energy 3. https://doi.org/10.1088/2515-7655/abee33

Nematollahi, D., Shayani-Jam, H., Alimoradi, M., Niroomand, S., 2009. Electrochemical oxidation of acetaminophen in aqueous solutions: Kinetic evaluation of hydrolysis, hydroxylation and dimerization processes. Electrochim. Acta 54, 7407–7415. https://doi.org/10.1016/j.electacta.2009.07.077

Ormeno-Cano, N., Radjenovic, J., 2022. Electrochemical degradation of antibiotics using flow-through graphene sponge electrodes. J. Hazard. Mater. 431, 128462.

Pacheco-Álvarez, M., Picos Benítez, R., Rodríguez-Narváez, O.M., Brillas, E., Peralta-Hernández, J.M., 2022. A critical review on paracetamol removal from different aqueous matrices by Fenton and Fenton-based processes, and their combined methods. Chemosphere 303. https://doi.org/10.1016/j.chemosphere.2022.134883

Pierpaoli, M., Dettlaff, A., Szopińska, M., Karpienko, K., Wróbel, M., Łuczkiewicz, A., Fudala-Książek, S., Bogdanowicz, R., 2021a. Simultaneous opto-electrochemical monitoring of carbamazepine and its electro-oxidation by-products in wastewater. J. Hazard. Mater. 419. https://doi.org/10.1016/j.jhazmat.2021.126509

Pierpaoli, M., Jakóbczyk, P., Dec, B., Giosuè, C., Czerwińska, N., Lewkowicz, A., Ruello, M.L., Bogdanowicz, R., 2022. A novel hierarchically-porous diamondized polyacrylonitrile sponge-like electrodes for acetaminophen electrochemical detection. Electrochim. Acta 430, 1–11. https://doi.org/10.1016/j.electacta.2022.141083

Pierpaoli, M., Jakobczyk, P., Sawczak, M., Łuczkiewicz, A., Fudala-Książek, S., Bogdanowicz, R., 2021b. Carbon nanoarchitectures as high-performance electrodes for the electrochemical oxidation of landfill leachate. J. Hazard. Mater. 401, 123407. https://doi.org/10.1016/j.jhazmat.2020.123407

Pierpaoli, M., Rycewicz, M., Łuczkiewicz, A., Fudala-Książek, S., Bogdanowicz, R., Ruello, M.L., 2020. Electrodes criticality: the impact of CRMs in the leachate electrochemical oxidation. Manuf. Rev. 7, 7. https://doi.org/10.1051/mfreview/2020006

Pierpaoli, M., Szopińska, M., Wilk, B.K., Sobaszek, M., Łuczkiewicz, A., Bogdanowicz, R., Fudala-Książek, S., 2021c. Electrochemical oxidation of PFOA and PFOS in landfill leachates at low and highly boron-doped diamond electrodes. J. Hazard. Mater. 403. https://doi.org/10.1016/j.jhazmat.2020.123606

Rajabpour, S., Mao, Q., Gao, Z., Khajeh Talkhoncheh, M., Zhu, J., Schwab, Y., Kowalik, M., Li, X., van Duin, A.C.T., 2021. Low-temperature carbonization of polyacrylonitrile/graphene carbon fibers: A combined ReaxFF molecular dynamics and experimental study. Carbon N. Y. 174, 345–356. https://doi.org/10.1016/j.carbon.2020.12.038

Randles, J.E.B., 1947. Kinetics of rapid electrode reactions. Discuss. faraday Soc. 1, 11–19.

Santos, J.E.L., Gomez, M.A., de Moura, D.C., Cerro-López, M., Quiroz, M.A., Martínez-Huitle, C.A., 2021. Removal of herbicide 1-chloro-2, 4-dinitrobenzene (DNCB) from aqueous solutions by electrochemical oxidation using boron-doped diamond (BDD) and PbO2 electrodes. J. Hazard. Mater. 402, 123850.

Shestakova, M., Sillanpää, M., 2017. Electrode materials used for electrochemical oxidation of organic compounds in wastewater. Rev. Environ. Sci. Biotechnol. https://doi.org/10.1007/s11157-017-9426-1

Siddique, R., Singh, G., 2011. Utilization of waste foundry sand (WFS) in concrete manufacturing. Resour. Conserv. Recycl. 55, 885–892. https://doi.org/10.1016/j.resconrec.2011.05.001

Tian, W., Zhang, H., Duan, X., Sun, H., Shao, G., Wang, S., 2020. Porous carbons: Structure-oriented design and versatile applications. Adv. Funct. Mater. 30, 1909265.

593   Wang, P., Hu, Y., Cheng, H., 2019. Municipal solid waste (MSW) incineration fly ash as an important source of
594   heavy metal pollution in China. Environ. Pollut. 252, 461–475.

595   Wilk, B.K., Szopińska, M., Sobaszek, M., Pierpaoli, M., Błaszczyk, A., Luczkiewicz, A., Fudala-Ksiazek, S.,
596   Krystyna, B., Malgorzata, W., Michał, S., Mattia, S., Agata, P., 2022. Electrochemical oxidation of landfill
597   leachate using boron-doped diamond anodes: pollution degradation rate, energy efficiency and toxicity
598   assessment. Environ. Sci. Pollut. Res. 1–17. https://doi.org/10.1007/s11356-022-19915-3

599   Wu, S., Zhang, L., Chen, J., 2012. Paracetamol in the environment and its degradation by microorganisms. Appl.
600   Microbiol. Biotechnol. 96, 875–884. https://doi.org/10.1007/s00253-012-4414-4

601   Zhang, Q., Cao, Y., Yan, Y., Yuan, B., Zheng, H., Gu, Y., Zhong, X., Wang, J., 2020. Synergetic effect of pyrrolic-N
602   and doped boron in mesoporous carbon for electrocatalytic ozone production. J. Mater. Chem. A 8, 2336–
603   2342. https://doi.org/10.1039/c9ta12866b

604   Zhang, Q., Yang, Y.-L., Zhou, Y., Hong, J., 2022. Paracetamol degradation via electrocatalysis with B and N co-
605   doped reduced graphene oxide: Insight into the mechanism on catalyst surface and in solution.
606   Chemosphere 287, 132070.

607   Zhang, Y., Wang, B., Cagnetta, G., Duan, L., Yang, J., Deng, S., Huang, J., Wang, Y., Yu, G., 2018. Typical
608   pharmaceuticals in major WWTPs in Beijing, China: Occurrence, load pattern and calculation reliability.
609   Water Res. 140, 291–300. https://doi.org/10.1016/j.watres.2018.04.056

610